Colloids and Surfaces B: Biointerfaces 264 (2026) 115665

Contents lists available at ScienceDirect

Colloids and Surfaces B: Biointerfaces

journal homepage: www.elsevier.com/locate/colsurfb

Lipid-phase-modulated interactions of gold nanoparticles with supported vesicular and planar membranes

Laure Bar [a,b,*], Marta Lavrič [b], Maja Caf [c,d], Slavko Kralj [c,d], Raj Kumar Sadhu [e], Miha Škarabot [b,f], Patricia Losada-Pérez [g], Aleš Iglič [a], George Cordoyiannis [b,**]

[a] Laboratory of Physics, Faculty of Electrical Engineering, University of Ljubljana, Ljubljana 1000, Slovenia
[b] Condensed Matter Physics Department, Jožef Stefan Institute, Ljubljana 1000, Slovenia
[c] Department for Materials Synthesis, Jožef Stefan Institute, Ljubljana 1000, Slovenia
[d] Faculty of Pharmacy, University of Ljubljana, Ljubljana 1000, Slovenia
[e] Department of Education, Indian Institute of Technology Kharagpur, Kharagpur 721302, India
[f] Faculty of Mathematics and Physics, University of Ljubljana, Ljubljana 1000, Slovenia
[g] Experimental Soft Matter and Thermal Physics Group, Department of Physics, Université Libre de Bruxelles, Brussels 1050, Belgium

ARTICLE INFO

Keywords:
Supported lipid vesicles
Supported lipid bilayers
Gold nanoparticles
Lipid phase
Quartz crystal microbalance with dissipation monitoring (QCM-D)
Nanoparticle-membrane interactions

ABSTRACT

The thorough understanding of the interactions between nanoparticles and lipid membranes has attracted major interest over the past few decades. This spans fundamental biophysics and biomechanics, as well as medical applications, where nanoparticles could serve as potential drug carriers. The influence of the lipid phase in these interactions has been studied to markedly less extent with respect to the nanoparticle size, shape and coating, as well as the presence of electric charge in either the nanoparticles or the membranes. Seeking to gain new insights into the lipid phase, we have systematically investigated the role of the liquid-disordered, the gel-ordered, as well as the seldom-studied ripple phases in modulating the interaction strength between nanoparticles and biomimetic membranes. Supported lipid vesicles and supported lipid bilayers of different composition and amount of electric charge, as well as spherical functionalized Au nanoparticles with and without charge have formed our experimental platform. The results, obtained by quartz crystal microbalance with dissipation monitoring and complemented by atomic force microscopy, reveal a strikingly different mechanistic picture of the interactions between the various lipid phases and types of nanoparticles. We demonstrate enhanced vesicle rupture in the case of stiffer membranes, consistent with recent theoretical studies, yet supported by limited existing experimental evidence. This work advances fundamental understanding of lipid-state-driven nanoparticle–membrane interactions. Such insight is essential, as dynamic changes in bilayer rigidity, composition, and surface charge determine how membranes and nanoparticles interact.

1. Introduction

The plasma membrane forms a complex boundary that protects the biological cell, regulates the transport of substances, and facilitates the communication with other cells and the surrounding environment. Each of its components, including phospholipids, glycolipids, peripheral and embedded proteins, as well as cholesterol and many more, contributes to the membrane's overall physicochemical behavior and its responses to external stimuli. The interactions of lipid membranes with various types of nanoparticles (NPs) have become an emerging field of research since the early 2000s. Major interest has developed in response to growing concerns regarding cell exposure to NPs and their potential cytotoxicity [1], as well as the use of NPs in biomedical applications as agents in diagnostics, theranostics and drug delivery [2]. Deep insights into the mechanisms behind the cell membranes and NPs interactions are essential before gaining targeted control over these processes [3,4]. Recent comprehensive reviews [5,6] summarize the interactions of several types of NPs – possessing variable core composition, size, and shape – with lipid membranes.

The membrane-NP interactions consist of a dynamic interplay between electrostatic and Van der Waals forces, hydrophobic interactions, hydrogen bonding and steric effects. Membrane curvature and degree of

* Corresponding author at: Laboratory of Physics, Faculty of Electrical Engineering, University of Ljubljana, Ljubljana 1000, Slovenia.
** Corresponding author.
E-mail addresses: laure.bar@fe.uni-lj.si (L. Bar), georgios.kordogiannis@ijs.si (G. Cordoyiannis).

https://doi.org/10.1016/j.colsurfb.2026.115665
Received 27 January 2026; Received in revised form 23 March 2026; Accepted 29 March 2026
Available online 30 March 2026

fluidity, as well as the NPs' size and shape also come into play [7]. Electrostatic forces acting over long or short distances drive the early stages of membrane interactions, facilitating adhesion [8–11]. NPs bearing positive charge target the mammalian cell membranes, which possess a global negative charge due to attached or embedded biomolecules. Strong electrostatic forces can lead to bilayer collapse referred to as toxicity effect. In contrast, anionic NPs experience repulsion from the negatively charged membrane, reducing their ability to disrupt and penetrate it. NPs also interact with the zwitterionic lipids of the membrane via hydrogen bonding or Van der Waals forces [12–14]. Note that zwitterionic phosphatidylcholine (**PC**) constitutes one of the predominant lipid heads at the outer leaflet of the cell membrane [15,16]. Wei et al. [13] observed that negatively charged SiO_2 NPs could instantly damage positively charged giant unilamellar vesicles (**GUVs**). Surprisingly, they also noticed that the same NPs could damage negatively charged GUVs after long incubation times of several hours, indicating that the interaction mechanisms extent beyond electrostatic forces. The outcomes of these complex interactions range from simple NP adhesion to complete vesicle rupture, depending on NP size and charge, and lipid vesicle composition. Smaller NPs, with diameter below 10 nm, tend to be internalized or create vesicle tubulations [17–19], whereas larger NPs adhere and deform the membrane [19]. NP aggregation on the lipid bilayer surface, engulfment, pore formation or membrane rupture can also be encountered [7,8,20–22]. Overall, diverse phenomena arise from the competition between NPs' adhesion energy per unit area and membrane bending rigidity [21]. Helfrich elastic energy, incorporating bending modulus and curvature, has been used to estimate whether NPs become fully, partially, or not wrapped by lipid membranes [10,23,24]. It is worth noting that, in experimental conditions, the interactions are influenced by additional parameters: the ionic strength of the buffer, the pH, and the presence of cations [9,25–27].

The impact of NPs' type, size, shape, surface coating and electric charge on their interactions with the membranes has quite often been studied using biomimetic (i.e. model) membranes such as lipid monolayers, supported lipid vesicles (**SLVs**) and supported lipid bilayers (**SLBs**) [5]. In particular, SLVs and SLBs possess certain advantages. They can be readily formed in a reproducible manner following well-established protocols, and mimic the structure of the biological membrane in a lower – yet well controlled and variable – degree of complexity. By modifying parameters, such as composition, amount of charge, and curvature, one can unravel their individual roles in NPs-lipid bilayers interactions and gain clear mechanistic insights.

In this work, we utilized quartz crystal microbalance with dissipation monitoring (**QCM-D**), a surface-sensitive and label-free method, to follow the formation of SLBs and SLVs and to investigate in real-time their interactions with gold nanoparticles (**Au NPs**) [28,29]. Atomic force microscopy (**AFM**) has also been used in a complementary manner. Neutral as well as negatively charged Au NPs were synthesized. Concurrently, SLBs and SLVs were prepared using zwitterionic PC-lipids, positively charged lipids, as well as mixed compositions. In particular, we used four zwitterionic PC-lipids, namely, 1,2-dimyristoyl-sn-glycero-3-phosphocholine (**DMPC**), 1,2-dipalmitoyl-sn-glycero-3-phosphocholine (**DPPC**), 1,2-distearoyl-sn-glycero-3-phosphocholine (**DSPC**), and 1,2-Dioleoyl-sn-glycero-3-phosphocholine (**DOPC**), as well as the positively charged lipid 1,2-Dioleoyl-3-trimethylammoniumpropane (**DOTAP**). As noted above, zwitterionic lipids provide a relevant model for membrane-mimicking systems. At the same time, although biological membranes are overall negatively charged, positively charged lipids are of significant scientific interest, as cationic lipid vesicles have been used in biomedical applications as effective drug-delivery carriers. In particular, they have been shown to enhance cellular uptake of liposomal complexes encapsulating quantum dots [30].

Substantial effort was put into the investigation of the role of lipid phase, which has thus far received limited attention [31], in contrast to size and charge effects that have been readily addressed [17,32]. As a matter of fact, some parts of the cell membranes, enriched in cholesterol and proteins, exhibit an increased, gel-like, rigidity. Lipids can also exist in the gel phase in certain parts of the human body, such as PC-lipids in the lungs, which undergo a phase transition during breathing due to pressure changes [33]. Therefore, the NPs' impact on stiffer gel membranes merits further investigation. Moreover, we explored the seldom-studied ripple phase, whose structure lies between that of the gel and liquid phases.

Two types of spherical Au NPs, with a core of ~ 10 nm, were functionalized with poly-ethylene glycol (**PEG**) chains of variable length. In one case, the PEG was terminated with a methoxy **(-OMe**) functional group to form neutral NPs (**Au-PEG-OMe NPs**); in the other case, the PEG was terminated with carboxy **(-COOH**) functional group to provide negatively charged NPs (**Au-PEG-COOH NPs**) at our working conditions. The use of Au NPs has certain advantages, such as high biocompatibility, very low chemical reactivity, and easy functionalization with a wide range of capping agents or drugs. Au NPs also absorb in the visible-near-infrared region, which renders them excellent imaging agents [34]. In addition, PEG functionalization prevents the aggregation of NPs, and increases their stability and dispersion within the aqueous medium (buffer) used in the experiments. Furthermore, compounds and NPs functionalized with PEGs have optimized pharmacokinetics in biological systems, since their clearance speed from blood circulation is reduced due to their low immunogenicity [35]. The SLBs' and SLVs' compositions of this work, as well as the amount of electric charge, have been systematically varied in a stepwise manner. This approach enabled us not only to determine, but also to decouple and isolate the impact of the lipid packing – differing across the liquid, ripple, and gel phases – on the interactions between model membranes and NPs.

2. Materials and methods

2.1. Lipids

SLBs and SLVs were formed using four zwitterionic PC-lipids (DMPC, DPPC, DSPC, and DOPC) and the positively charged DOTAP, as stated in the introduction. DMPC, DPPC and DSPC bear the same PC-head, whereas their acyl chain lengths differ by two carbon atoms (in total 14, 16 and 18 carbon atoms respectively). All lipids were purchased from Avanti Polar Lipids (Alabaster, USA), in powder form, and always kept at −20 °C.

Tris(hydroxymethyl)aminomethane (**Tris**) buffer was used in all experiments and was freshly prepared on a weekly basis. Trizma base powder ≥ **99.9%** and NaCl ≥ **99%**, purchased from Sigma Aldrich (Steinheim, Germany), were dissolved in Milli-Q water to reach concentrations of 10 mM and 150 mM respectively. Milli-Q water, with a resistivity of 18.2 MΩ·cm at 25 °C, was freshly purified prior to each experiment using a Milli-Q® SQ 2Series (Merck Millipore, Overijse, Belgium). The pH of the buffer was then gradually reduced to 7.4 by adding a tiny volume of diluted HCl; the pH values were monitored by a Metrohm 827 Lab pH-meter (Herisau, Switzerland). Next, the buffer solution was filtered through 0.2 μm-pore size polyethersulfone membranes (Corning GmbH - Wiesbaden, Germany) and stored at 4 °C until being used. For the extrusion of lipid suspensions, a mini-extruder kit from Avanti Polar Lipids, as well as 100 nm-pore polycarbonate membranes and filter supports from Cytiva Whatman™ were used. High-purity isopropanol (**IPA**), purchased from VWR Chemicals (Leuven, Belgium), was used to form SLBs.

2.2. Preparation of supported lipid vesicles (SLVs) and supported lipid bilayers (SLBs)

Two types of biomimetic membranes were used, namely, SLVs of 100 nm diameter, as well as SLBs. For the experiments involving SLVs, suspensions of lipid unilamellar vesicles were prepared. Initially, the lipids of interest (or mixtures of different lipids) in powder form were

dissolved in high-purity (> **99.9%**) chloroform, which was then slowly evaporated under a mild flow of argon in order to form dry lipid films. The films were kept vented overnight to ensure the elimination of any solvent residues. In the next day, they were hydrated for 45 min with Tris buffer to a concentration of 2 mg/mL. The hydration was performed at elevated temperatures corresponding to the liquid-disordered phase, by immersing the vials in a hot water bath. The temperature of the latter was kept homogeneous by continuous magnetic stirring. The large multilamellar vesicles formed during this process were then extruded through polycarbonate membranes with pore size of 100 nm, operating a series of 25 passes, to become unilamellar and monodisperse. Finally, the obtained suspensions were diluted in buffer to a concentration of 0.5 mg/mL and injected into the QCM-D modules with a flow rate of 50 μL/min. Dynamic light scattering (**DLS**) and zeta (ζ) potential measurements were used for the characterization of vesicles' size, as well as electric charge (see Supplementary Material).

The SLBs were prepared using the solvent-exchange method, also referred to as *solvent-assisted lipid bilayers* (**SALB**) formation method [36,37]. In this case, one starts the sample preparation by dissolving the lipid in an organic solvent that is miscible with the aqueous buffer. Lipids in powder form were dissolved at a concentration of 0.5 mg/mL in high-purity IPA; the latter was reported to yield optimum results [38]. The solutions (lipids in IPA) were prepared and sonicated for 2 min just before the injection into the QCM-D modules. The solvent-exchange, from IPA-to-Tris, was performed inside the modules, using a flow rate of 100 μL/min, until stable plateaus were formed at frequency values around –25 Hz corresponding to single homogeneous SLBs.

2.3. Synthesis, functionalization and characterization of gold nanoparticles (Au NPs)

Au NPs were synthesized according to our previously published protocol [39], and their functionalization procedures are described in detail in the Supplementary Material. The characterization of nanoparticles was performed by DLS, ζ potential measurements, as well as transmission electron microscopy (**TEM**). TEM analysis was carried out using a JEOL microscope equipped with energy-dispersive X-ray spectroscopy (EDXS, JEM 2100, Japan). TEM grids were prepared by drop-casting several aliquots of the diluted nanoparticle suspensions onto carbon-coated copper grids, followed by air drying at room temperature. Particle size distribution was determined using ImageJ software, based on the manual analysis of a representative sample of $N = 500$ individual particles. For these measurements, nanoparticle suspensions were diluted to a final concentration of 200 μg/mL in the appropriate solvents and transferred into disposable cuvettes for analysis under standard conditions. The results obtained from these measurements are included in Figure S1 (Supplementary Material).

2.4. Quartz crystal microbalance with dissipation monitoring (QCM-D)

A four-module QSense Analyzer (Biolin Scientific, Sweden) QCM-D was employed for probing in real-time the interactions between SLBs and SLVs with different types of Au NPs. The setup operates between 15 °C and 60 °C, and allows the simultaneous execution of four experiments. In the heart of each module lies an AT-cut quartz sensor, which can possess variable surface coatings according to the needs of individual experiments; in the present work, Au-coated sensors (QSense QSX 301) have been used for SLVs and SiO_2 ones (QSense QSX 303) for SLBs. Prior to the experiments, these sensors were cleaned in line with the standard recommended protocols. The samples were injected into the modules using a peristaltic pump with adjustable flow rates. Frequency and dissipation data were collected for the fundamental frequency (5 MHz) and odd overtones. The extraction and fitting of experimental data were performed utilizing QSoft 2.8.6 and DFind 1.3.0 software provided with the experimental setup.

2.5. Atomic force microscopy (AFM)

AFM measurements were performed using a MultiMode 8 microscope (Bruker, USA). Imaging was performed in buffer using the Peak Force mode and ScanAsyst-Fluid probes with a cantilever length of ~ 70 μm, a resonance frequency of ~ 150 kHz, and a spring constant of ~ 0.7 N/m. The large tip radius of 20 nm enables a gentle surface scanning, limiting vesicle damage. To ensure that AFM measurements were performed under the same conditions as the QCM-D experiments, each surface was first prepared within QCM-D module. The sensors were then directly transferred and examined by AFM, either after lipid adsorption and rinsing, or after an additional nanoparticle injection and rinsing step. The samples were transferred from QCM-D to the AFM fluid cell with care to remain constantly hydrated. Images were obtained using 512 × 512 pixels sampling, 0.5 Hz scan rate, and 280 pN setpoint force.

2.6. Simulations

Our simulation model is based on a coarse-grained continuum model, where the flexible membrane of a vesicle is described as a two-dimensional surface formed by using triangles [7,40]. This model nicely captures the efficient membrane encapsulation of colloidal particles driven by curved membrane proteins and active cytoskeleton forces [7], the cell/vesicle spreading and migration on flat and curved surfaces [40,41], as well as coiling of cell's leading edge on fibers. The vesicle possesses a bending energy which gives it a tendency to remain locally as flat as possible. Moreover, the vesicle is placed on an adhesive substrate having attractive interaction with the vertices of the triangles of the vesicle. The vertices of this triangulated surface can move as well as diffuse on the membrane surface by random Monte Carlo moves, in such a way that tends to minimize the overall energy (bending + adhesion) of the vesicle with time. We varied the bending rigidity κ of the membrane and obtained the corresponding equilibrium shapes by running the simulation for long timescales.

3. Experimental results

In this section, we present the experimental results, obtained by means of QCM-D, on a series of samples. In the first subsection 3.1, the results obtained on the Au NPs interactions with SLBs – as the initial testbed of lowest complexity – are presented. Our main results on neutral and charged Au NPs interacting with SLVs are presented in subsections 3.2 and 3.3 respectively.

3.1. Interactions of functionalized Au NPs with SLBs

Neutral and positively charged planar SLBs were used to probe the impact of charge on the NP–membrane interactions under the simplest conditions: same lipid phase, no curvature, and no acyl chain length mismatch in the mixed bilayers. Note that, henceforth, when used for lipids, the term 'neutral' refers to zwitterionic lipids with overall net charge of approximately zero. Three different types of SLBs were formed using the SALB method (described in the previous section): pure DOPC (neutral), DOPC:DOTAP with a 50:50 molar ratio (partially positively charged), and pure DOTAP (positively charged). The SLB formation was followed in real-time by QCM-D (an example of DOPC SLB formation can be found in Figure S2 of Supplementary Material); the bilayer quality was confirmed by the final frequency ($\Delta f_n/n$) and dissipation (ΔD_n) shifts. A homogeneous, defect-free lipid bilayer typically exhibits a frequency shift plateau value of around –25 Hz and low dissipation shifts in the order of 10^{-6} [36,37,42]. In addition, all the normalized frequency ($\Delta f_n/n$) and dissipatation (ΔD_n) overtones overlap indicating a homogeneous bilayer.

Fig. 1 displays the response of the aforementioned SLBs upon the addition of Au-PEG-OMe and Au-PEG-COOH NPs. In the case of neutral DOPC SLBs and neutral Au-OMe NPs (values of zeta potential, ζ, shown

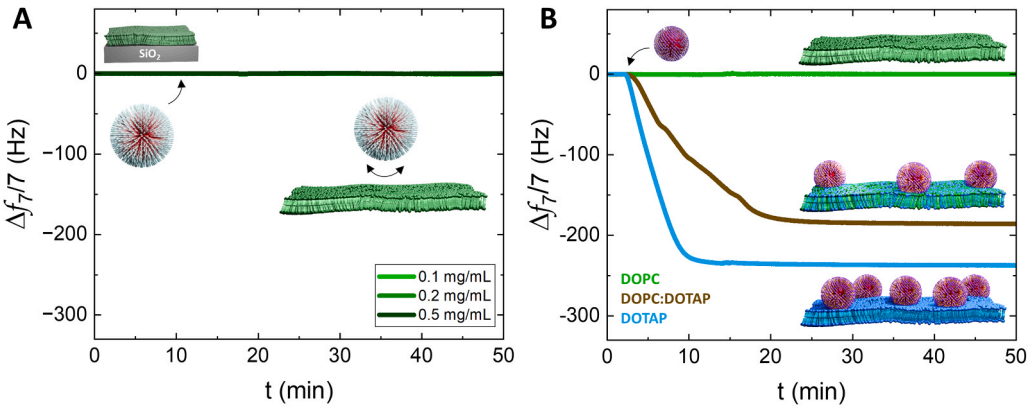

Fig. 1. Panel A: the $\Delta f_n/n$ ($n = 7$) changes observed upon the addition of three concentrations (0.1, 0.2, and 0.5 mg/mL represented by light, medium and dark green curves respectively) of Au-PEG-OMe NPs, onto DOPC SLBs; the three curves essentially overlap. Panel B: the $\Delta f_n/n$ ($n = 7$) changes observed upon the addition of Au-PEG-COOH NPs (concentration of 0.2 mg/mL) onto DOPC, DOPC:DOTAP 50:50, and DOTAP SLBs represented by green, brown, and blue color curves respectively. In all cases, experiments were performed at 37 °C using Tris buffer (pH ≈ 7.4), a flow-rate of 50 μL/min, with SLBs being supported on a SiO_2 substrate. The same scale along the vertical (frequency) axis is used in both panels for comparison.

in Table S1 and Table S2 of Supplementary Material), presented in Fig. 1A, there is no interaction observed for different NP concentrations (0.1, 0.2, and 0.5 mg/mL) injected with the same flow rate (50 μL/min). The oscillation frequency remains essentially unaffected by the injection, independently of the NPs' concentration. This is in line with the absence of any NP adsorption, due to the lack of (or too weak) electrostatic interactions.

The results in the case of negatively charged NPs and neutral or (partially) charged SLBs are presented in Fig. 1B. The Au-PEG-COOH NPs ($\zeta = -39.5 \pm 1.2$ mV) have been injected on DOPC ($\zeta = -0.3 \pm 1.4$ mV), DOPC:DOTAP 50:50 ($\zeta = 28.7 \pm 1.2$ mV), and DOTAP ($\zeta = 42.1 \pm 2.6$ mV) SLBs. When the Au-PEG-COOH NPs were injected on neutral DOPC, there was no frequency shift as also observed in the case of neutral NPs and SLBs (Fig. 1A). On the contrary, for DOPC:DOTAP 50:50 and pure DOTAP SLBs, a strong frequency downshift was observed characteristic of mass uptake. This downshift was more pronounced and occurred in a shorter time scale (i.e. faster kinetics) for pure DOTAP. Therefore, as the SLB's positive surface charge density increased, the strength and the rate of negatively charged NPs adsorption increased accordingly, assumed to be driven by electrostatic interactions. A similar trend as a function of charge density was observed in our previous study on the interactions of negatively charged CdTe quantum dots (QDs), also functionalized with capping agents terminated by a COOH group, with positively charged DOPC:DOTAP and DOTAP SLBs [43]. A quantitative comparison of the Au-PEG-OMe NPs (this work) and CdTe QDs (from Ref. [43]) can be found in Figure S3 (Supplementary Material). The Au-PEG-OMe NPs exhibit a larger mass uptake that could be attributed to: (i) the larger core size (~ 10 nm for Au NPs versus ~ 5 nm for CdTe QDs) and higher material density, and (b) the more negative ζ potential (−40 mV for Au-PEG-COOH versus −24 mV for CdTe-COOH) and, thus, the stronger electrostatic attraction between them and same positively charged SLBs. These results confirm the impact of electric charge in the interaction of Au NPs with planar membranes; in the following two subsections, we address the NP-lipid interactions in membranes possessing curvature, specifically in 100 nm vesicles.

3.2. *Interactions of neutral Au NPs with zwitterionic SLVs at different phases*

We hereby present results on the interactions of zwitterionic SLVs with different compositions and neutral Au-PEG-OMe NPs. Three PC-lipids were used as vesicle components, DMPC, DPPC and DSPC, with increasing acyl chain length and phase transition temperatures. The main transition anomalies occur at 24.6 ± 0.3 °C, 42.1 ± 0.2 °C, and 55.4 ± 0.3 °C, as shown in Figure S4 (Supplementary Material). Therefore, the three particular lipids were intentionally chosen for the experiments conducted at 37 °C, in order to work with SLVs in three different phases: liquid, ripple, and gel. At 37 °C, DMPC is in the liquid phase, DPPC in the ripple phase, and DSPC in the gel phase respectively. In order to ensure monodisperse and unilamellar vesicle populations, extrusion was performed using 100 nm pore membranes as defined in Materials and methods section. The experiments were performed in two steps that included: (i) the injection of freshly-extruded lipid suspensions onto Au-coated quartz sensors to form homogeneous SLVs, and (ii) the subsequent addition of NPs to monitor their interactions with SLVs.

Fig. 2 illustrates the frequency and dissipation changes (overtones $n = 3$–9) recorded during the two step-experiments performed at 37 °C for the three different SLVs. The flow rate was set to 50 μL/min for forming the SLVs, and was then reduced to 25 μL/min for the NPs injection. Clear differences were observed already at the SLV formation, since by increasing the carbon chain length, the frequency and dissipation shifts became more pronounced. In particular, the average $\Delta f_n/n$ and ΔD_n shifts were −196 ± 20 Hz and (32 ± 3) × 10^{-6} for DMPC, −353 ± 21 Hz and (40 ± 7) × 10^{-6} for DPPC, and −369 ± 22 Hz and (45 ± 8) × 10^{-6} for DSPC respectively. The increasing vesicles' membrane stiffness from DMPC, to DPPC and DSPC led to a reduced degree of deformation (bending and stretching) upon vesicle adsorption. To better demonstrate the behavior of adsorbed vesicles possessing variable stiffness, Monte Carlo simulations of the membrane dynamics were performed. The equilibrium shapes of supported large unilamellar vesicles were analyzed under different arbitrary bending rigidity (κ) values, ranging from 20 k_BT to 100 k_BT, k_B being the Boltzmann constant. Equilibrium shapes for four different values of κ are presented in the panels of Fig. 3, and links for videos of the simulations are available in the Supplementary Material.

Vesicles of higher bending rigidity (i.e. higher κ values) adhere to surfaces with only minor shape changes, in contrast to those of lower bending rigidity, which undergo significant deformations. This difference arises from the molecular packing of the lipids. Typically, lipid monomers in the gel phase are tightly packed and well-ordered, rendering the membranes rigid and more resistant to bending. Vesicles composed of lipids being in the gel-ordered phase – such as DSPC at 37 °C – are associated to the higher bending rigidity values in Fig. 3, referred to as 'stiff' and 'rigid' throughout the manuscript. On the contrary, lipid monomers in the liquid phase have their tails disordered and loosely packed, rendering the membranes more fluid and easy to deform. Vesicles composed of lipids being in liquid-disordered phase – such as DMPC at 37 °C – are associated to the lower bending rigidity values in Fig. 3, hereinafter referred to as 'soft' and 'flexible'. This reduced bending rigidity allows a larger adhesion contact area between

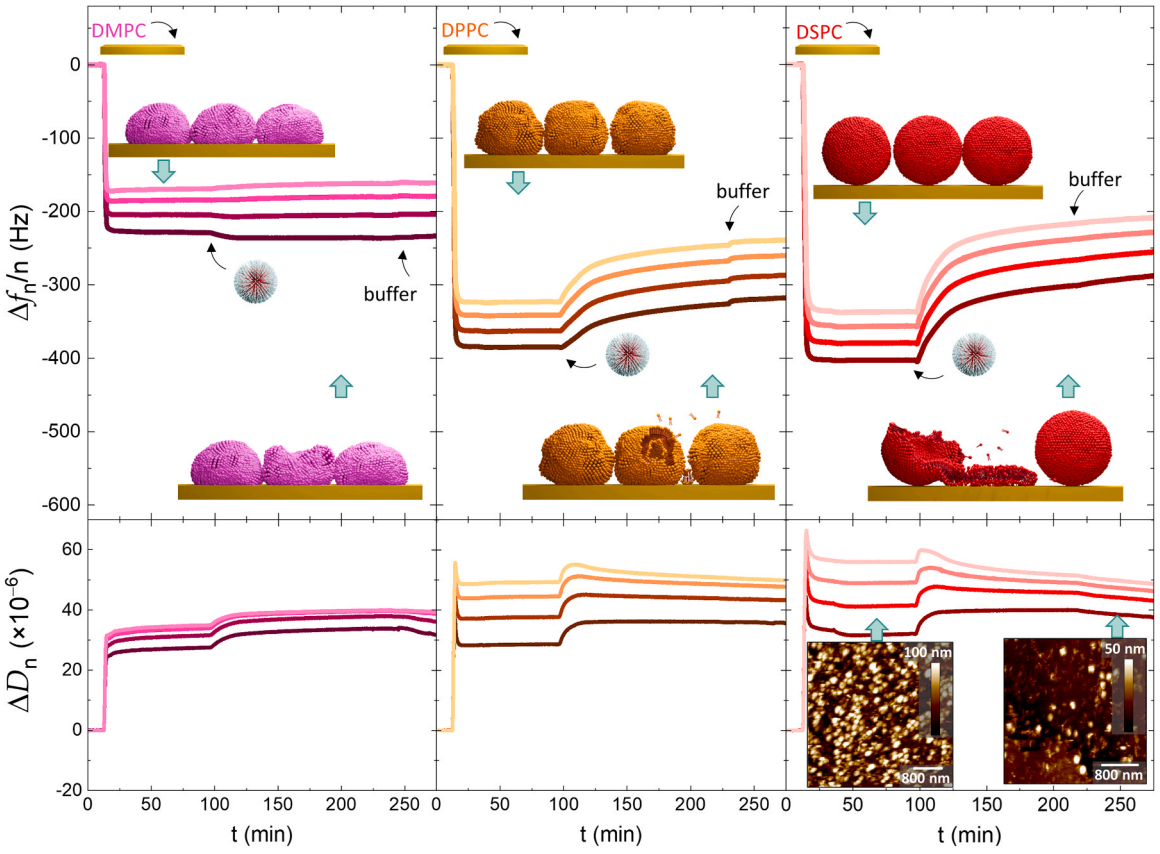

Fig. 2. The formation of DMPC (pink color, left column), DPPC (orange color, central column), and DSPC (red color, right column) zwitterionic SLVs on Au substrates and subsequent interaction with neutral Au-PEG-OMe NPs probed by QCM-D. The changes in $\Delta f_n/n$ (upper part) and ΔD_n (lower part) were recorded for overtones $n = 3$–9, with the color progressively changing from darker ($n = 3$) to lighter ($n = 9$). The vesicles extruded through 100 nm-pore membranes, were injected at 0.5 mg/mL in Tris buffer at a flow rate of 50 μL/min, whereas the NPs were injected at a concentration of 0.2 mg/mL at a flow rate of 25 μL/min (also in Tris buffer). Both steps were performed at 37 °C, allowing DMPC, DPPC, and DSPC SLVs to be in the liquid, the ripple and the gel phases respectively. Schemes illustrating the observed phenomena are shown for each case. The two insets for DSPC show additional AFM topographical images that support the QCM-D findings.

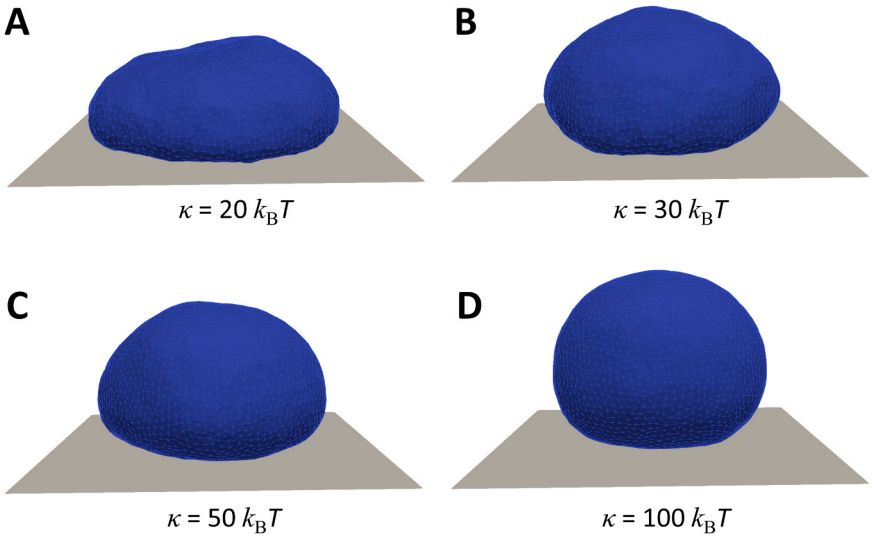

Fig. 3. Monte Carlo simulations of membrane dynamics showing the equilibrium shapes of the lipid vesicles depending on the bending rigidity κ; panel A: 20 k_BT; panel B: 30 k_BT; panel C: 50 k_BT; panel D: 100 k_BT. The adhesion between the membrane and substrate is 1.0 k_BT per node.

the vesicle and substrate, leading to a more pronounced flattening of the vesicles. In QCM-D realm, this translates to DMPC vesicles deforming their shape and spreading more across the sensor surface, eventually resulting in fewer adhered vesicles per area compared to DPPC and (even fewer than) DSPC. The DMPC SLVs will also be thinner compared to their DPPC and (even thinner than) DSPC counterparts. This explains the trends in the frequency and dissipation shifts seen from left to right in Fig. 2. The physical behavior of the ripple phase resembles that of the

gel-ordered phase, indicating somewhat similar mechanical properties. Using the viscoelastic models of DFind and QTools software, from two different QCM-D setups, we have obtained average SLV thickness of 92 ± 5 nm (DMPC), 107 ± 11 nm (DPPC), and 114 ± 14 nm (DSPC). For comparison, the diameters of vesicles in solution (i.e. before the adsorption), determined by DLS, were 128 ± 3 nm (DMPC), 133 ± 4 nm (DPPC) and 125 ± 3 nm (DSPC) respectively. Thus, the softer the vesicles' membranes (i.e. lower bending rigidity), the larger their shape change upon adsorption, in line with the trends displayed by Monte Carlo simulations (Fig. 3). We will return, in the Discussion section, to the importance of vesicle membrane stiffness in the interactions with Au NPs.

In all experiments, the suspensions of neutral Au-PEG-OMe NPs were injected at t = 100 min. On DMPC SLVs (left panel of Fig. 2), only mild changes and mostly in the lower $\Delta f_n/n$ overtones were observed. This indicates minor disturbance limited to the part of the vesicle layers away from the substrate and no actual NP adsorption. However, an increase in all dissipation overtones was noticed, indicating changes in the viscoelastic properties of the SLVs due to perturbation of their hydration environment. Even in the absence of electrostatic interactions, the injection of Au-PEG-OMe NPs rendered the SLV more dissipative and apparently less uniform.

In contrast to DMPC, an increase of all $\Delta f_n/n$ overtones in DPPC and DSPC (middle and right panels of Fig. 2) occurred after the injection of Au-PEG-OMe NPs, stabilizing at smaller (in absolute value) plateau values. This suggests a local vesicle membrane rupture, resulting in a layer composed of intact vesicles mixed with bilayer patches. This interpretation is further supported by AFM images shown in the insets of Fig. 2, as well as in Figure S5 of the Supplementary Material. These systems exhibited a larger variation between the ΔD_n overtones indicating a pronounced conformational restructuring. The lower ΔD_n overtones ($n = 3, 5$) increased to some plateau, whereas the higher ones ($n = 7, 9$) were initially destabilized albeit returning towards the previous plateau values. It is worth noting rupture events are solely attributed to the presence of NPs in the injected solution. This is supported by flushing the SLV with pure buffer at the same flow rate prior to NP injection (in all experiments), which caused no changes in frequency or dissipation signals, thereby leaving the SLV intact. In addition, repeated experiments demonstrated consistent reproducibility, as illustrated by one triplicate example (interactions of DSPC SLVs with Au-PEG-OMe NPs) shown in Figure S6 of the Supplementary Material.

A graphical comparison of the percentage (%) change of average frequency and dissipation shifts for DMPC, DPPC and DSPC after Au-PEG-OMe NPs injection – with respect to the initial shifts – is presented in the bar charts of Fig. 4A. The $\Delta f_n/n$ signal for DMPC – being in the liquid-disordered phase – remains essentially unaffected. In contrast, for DPPC in the ripple phase, $\Delta f_n/n$ exhibits a ~ **20%** loss of the initial shifts during the SLVs' formation, and for DSPC in the gel phase, an even greater loss of ~ **31%**. These results suggest that, for zwitterionic vesicle layers, an increasing membrane phase-dependent stiffness (DMPC being in the liquid, DPPC in the ripple, and DSPC in the gel phase at 37 °C) correlates with a higher susceptibility to membrane disruption by neutral NPs, as it will be discussed in the next section. Regarding dissipation, DMPC vesicles display an increase, presumably due to reorganization of the phospholipid hydration shell. For DPPC and DSPC vesicles, values at higher overtones ($n = 7, 9$), sensing closer to the substrate, differ from those at lower overtones ($n = 3, 5$), sensing farther away. Vesicle restructuring and rupture, as well as formation of supported bilayers and patches, especially pronounced for DSPC, caused the higher overtones to exhibit smaller – or even reversed – values compared to the lower ones.

An additional way to detect how lipids differ from one another is by plotting ΔD_n versus $\Delta f_n/n$, as depicted in Fig. 4B. In such a plot, one can distinguish two steps. Step (i.) shows the soft DMPC vesicles deforming quickly and spreading to uniformly cover the surface; stiffer DPPC and DSPC vesicles adsorbing more randomly, forming heterogeneous layers (maximum ΔD_n reached), and then rearranging to optimize the surface coverage. Step (ii.) corresponds with NPs' injection. DMPC exhibits a rapid rise in dissipation due to vesicles' deformation. DPPC has a similar rise in dissipation that later on flattens, indicating an initial interaction with the vesicles membrane surface preceding rupture. DSPC exhibits a mild and close-to-horizontal shift, suggesting immediate rupture of vesicles with no time for membrane reorganization.

It is worth noting the important role of the chosen flow rate for NPs injection; the latter was executed using two flow rates: 50 μL/min and 25 μL/min (Figure S7, in Supplementary Material). Interestingly, the interactions observed at 50 μL/min were milder, as illustrated by the significantly smaller signal variations. This very likely originates from the overall neutral charge of SLVs and NPs. In the absence of electrostatic attraction, the interactions essentially depend on weak forces (e.g. Van der Waals, hydrogen bonds) and passive diffusion of NPs. Therefore, a slower flow rate allows the NPs to stay for longer time scales near SLVs, increasing the chances of stochastic encounters.

The presented results show that, even in the case of weak or absent electrostatic attraction, interactions between NPs and SLVs still occur and disturb the organization of the latter, unlike what was obtained for planar membranes (i.e. SLBs in previous subsection). For stiffer vesicles (DPPC in the ripple phase and DSPC in the gel-disordered phase at 37 °C) the NPs cause a partial vesicle rupture. At this point, one could raise important questions: are these differences in the degree of interactions primarily governed by the vesicles' phase state, and therefore their membrane stiffness? Or could the varying acyl chain length of DMPC, DPPC, and DSPC, which subtly influences the bilayer thickness, also play a role? To clearly distinguish between these two possible effects, we

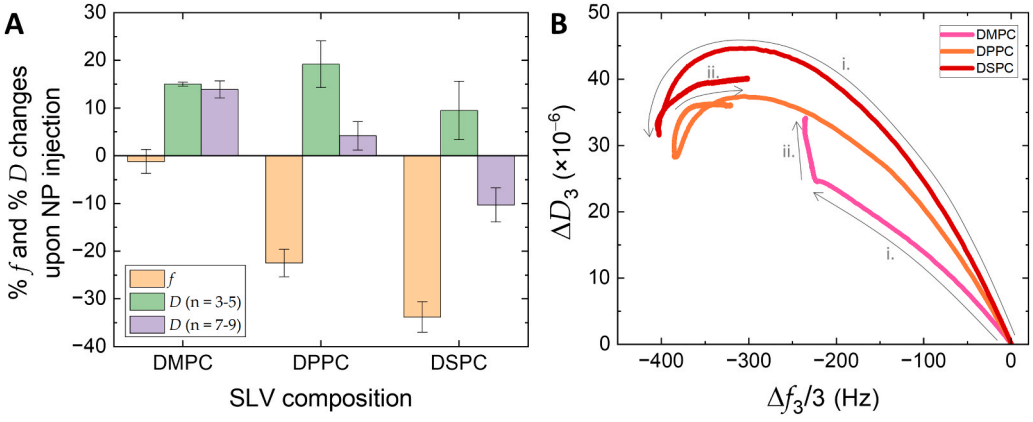

Fig. 4. Panel A: chart bars denoting the % change of $\Delta f_n/n$ and ΔD_n observed during the NPs' injection, relative to the initial shifts of SLVs formation. Panel B: plot of ΔD_n versus $\Delta f_n/n$ ($n = 3$), marking two steps during the experiment; step (i.) refers to the vesicle layer formation, and step (ii.) refers to the SLVs-NPs interactions.

conducted the same experiment using this time only DPPC vesicles at different temperatures (25 °C, 37 °C, and 50 °C), corresponding to the gel-ordered, the ripple, and the liquid-disordered phases respectively. This way we could isolate the impact of the membrane phase while keeping the lipid composition constant.

The results are presented in the two panels of Fig. 5, where the $\Delta f_n/n$ and ΔD_n shifts are shown for the two steps (DPPC SLV formation and interactions after NPs' injection). Regarding SLV formation, the shifts are noticeably smaller when DPPC is adsorbed at higher temperatures, as also observed in previous experimental studies [44]. As discussed earlier, this is due to the softer and more deformable vesicles resulting to lower hydrated mass adsorbed onto the substrate. The differences between 37 °C (onset of ripple phase) and 25 °C (gel-ordered phase) are less pronounced, because both phases maintain a relatively solid-like behavior compared to the liquid-disordered phase at 50 °C. In the gel phase, lipids are tightly packed, leading to a more rigid structure and a less dissipative energy. However, in the ripple phase, periodic undulations along the lipid bilayer can increase the energy dissipation as depicted in Fig. 5B.

Au-PEG-OMe NPs were injected on DPPC SLVs at the three mentioned temperatures, 25 °C, 37 °C, and 50 °C. At 50 °C, the frequency underwent – on average – a slight decrease, whereas dissipation a mild increase. Significantly larger and faster changes were observed at 37 °C and even more at 25 °C (largest shifts). More specifically, approximately −30 ± 3% of the frequency shift observed during SLV formation was lost following the NPs' injection at 25 °C, while a loss of around −23 ± 3% occurred at 37 °C. The observed trends closely resemble those in previous experiments (conducted at the same temperature) corresponding to different phases of the zwitterionic lipids DMPC, DPPC, and DSPC, which exhibited changes of less than −3.4 ± 1.0% for DMPC (liquid-disordered), around −23 ± 3% for DPPC (ripple), and −34 ± 3% for DSPC (gel). Therefore, the results presented in Fig. 2 and Fig. 5 demonstrate that vesicle rupture due to weak SLVs-NPs interactions is mainly governed by the lipid phase and packing rather than by the lipid chain length. Additional frequency and dissipation overtones from all three experiments shown in Fig. 5 are displayed in Figure S8 of the Supplementary Material.

Regarding the kinetics of the interactions, they can be probed by the slope of the frequency change upon NPs' injection. Linear fits were performed on the data of the initial five minutes right after injection. In the inset of Fig. 5**A**, the curves for overtone $n = 3$ were baseline-aligned to enhance the visualization of changes induced by the interactions with Au-PEG-OMe NPs. The fits revealed an initial frequency increase rate of 2.0 ± 0.5 Hz/min at 37 °C and 4.6 ± 0.6 Hz/min at 25 °C. Therefore, the rupture is not only more pronounced in the gel phase, but also occurs more rapidly.

3.3. Interactions of charged Au NPs with SLVs of variable amount of charge

Next, we investigated the SLVs interactions with NPs by incorporating electric charge in vesicles being in each phase to probe the interplay between lipid phase and charge. In order to assess the individual contribution of each parameter (i.e. phase or charge), we employed a stepwise approach. We first used SLVs being in the same phase yet displaying different amount of surface charge, followed by a comparative set of experiments involving variations in the phase while keeping the charge constant. In the first case, negatively charged Au-PEG-COOH NPs were injected on DOPC (neutral), DOPC:DOTAP 80:20 (partially charged), and DOTAP (fully charged) SLVs formed on Au substrates. Due to the low melting points, which are below 0 °C for both DOPC and DOTAP, these three types of SLVs are in the liquid phase at the chosen adsorption temperature of 37 °C. In the second case, the same Au-PEG-COOH NPs were injected on DMPC:DOTAP 80:20, DPPC:DOTAP 80:20, and DSPC:DOTAP 80:20 SLVs (i.e. all partially positively charged). At 37 °C, these SLVs are in the liquid-disordered, at the boundary of the ripple phase (along the main transition) and gel-ordered phases respectively (Figure S10 in the Supplementary Material). In all cases, a flow rate of 50 μL/min was employed for both steps, i.e. the formation of SLVs and the injection of NPs.

The adsorption of both DOPC and DOPC:DOTAP 80:20 vesicles led to frequency and dissipation plateau values corresponding to soft SLVs as depicted in Fig. 6 (with similar properties as for DMPC in the liquid-disordered phase, shown earlier in Fig. 2). On the contrary, for DOTAP, the QCM-D signal was characterized by slightly separated overtones with average shifts of –26.1 ± 2.4 Hz (frequency) and (4.0 ± 0.6) × 10^{-6} (dissipation) calculated from the overtones $n = 3$–9. These values are associated to inhomogeneous SLBs rather than SLVs. Apparently, due to its positive nature, DOTAP interacted strongly with the Au substrate bearing a negative charge at neutral pH [45]. As a result, the fully positively charged vesicles were prone to rupture upon adsorption, leading to the formation of a planar bilayer. The relatively large dissipation indicated that imperfections, such as non-ruptured vesicles or bilayer patches with exposed edges, were still present. The formation of this heterogeneous structure was reproducible across replicate experiments, as shown in Figure S9 of the Supplementary Material. Notably, on

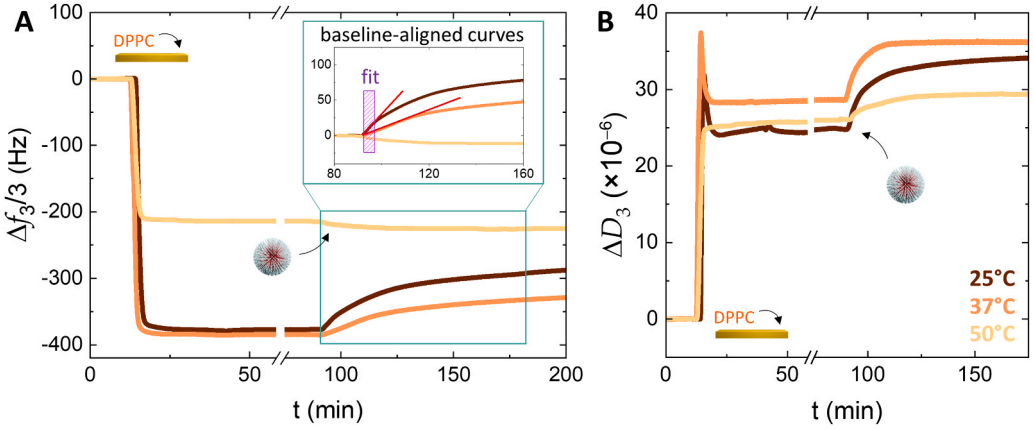

Fig. 5. The influence of the lipid phase on the SLVs-NPs interactions is depicted. $\Delta f_3/3$ (panel A) and ΔD_3 (panel B) curves are obtained by the injection of DPPC vesicles on Au-coated sensors, at a concentration of 0.5 mg/mL in Tris buffer (flow rate = 50 μL/min), followed by the Au-PEG-OMe NPs' injection at 0.2 mg/mL in Tris, (flow rate of 25 μL/min). The experiments were performed at 25 °C (brown curves, DPPC in the gel-ordered phase), 37 °C (orange curves, DPPC in the ripple phase) or 50 °C (yellow curves, DPPC in the liquid-disordered phase). The inset in panel A focuses on the NPs' injection step, where all curves are baseline-aligned for an easier comparison of the $\Delta f_3/3$ changes due to the SLVs-NPs interaction. Red lines are indicative extrapolated linear fits performed on the data of only the five first minutes of the injection (highlighted by a violet rectangle).

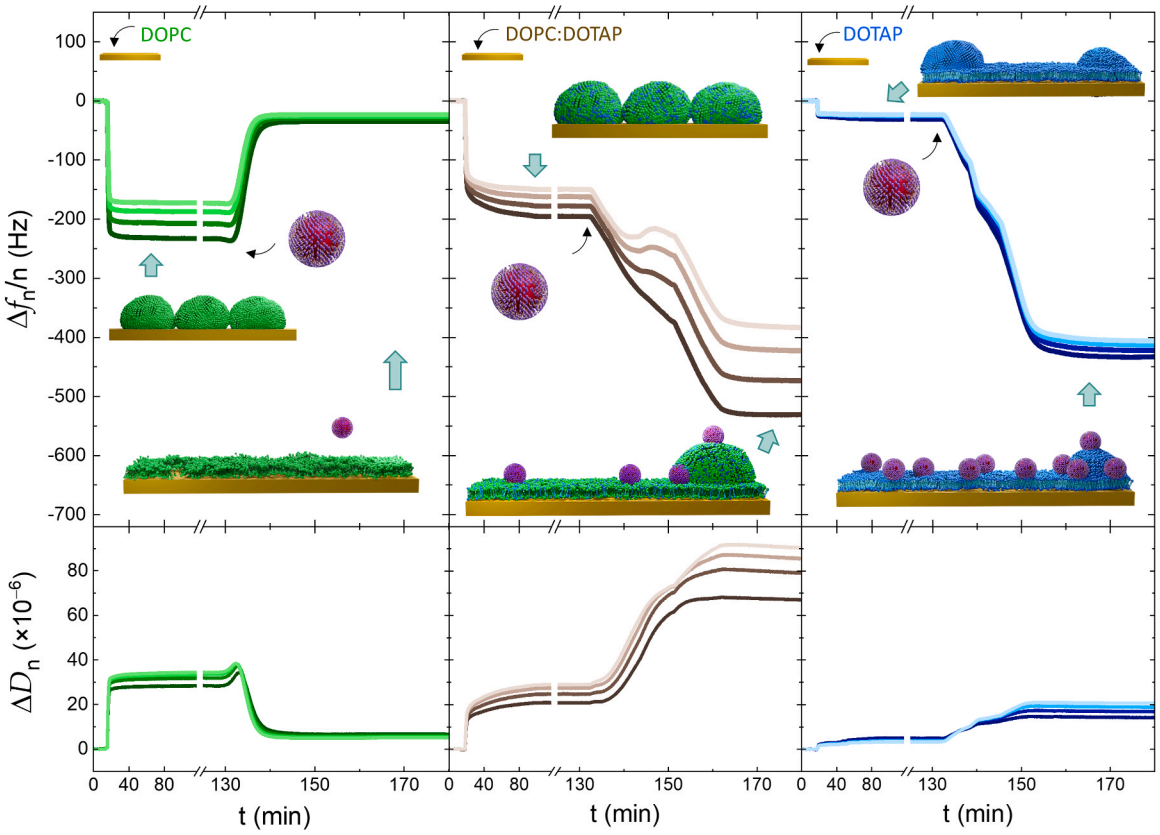

Fig. 6. Formation of DOPC (green curved, left column), DOPC:DOTAP 80:20 (brown curves, central column), and DOTAP (blue curves, right column) SLVs on Au quartz sensors and subsequent interaction with negatively charged Au-PEG-COOH NPs followed by QCM-D. The changes in $\Delta f_n/n$ (upper part) and ΔD_n (lower part) were monitored for the overtones 3–9; the color gradient of the curves corresponds to these overtones, ranging from darkest ($n = 3$) to lightest ($n = 9$). The 100 nm vesicles, were injected at 0.5 mg/mL in Tris buffer (flow rate = 50 μL/min), whereas the NPs were injected at 0.2 mg/mL in Tris (flow rate = 50 μL/min). Both steps were performed at temperature of 37 °C, at which all types of SLVs, DOPC, DOPC:DOTAP 80:20, and DOTAP, were in the liquid phase.

substrates with higher surface energy than Au, such as SiO_2, adsorbed DOTAP vesicles undergo complete rupture to form homogeneous SLBs [43]. On Au, however, vesicle rupture remains incomplete, yielding a mixed structure.

Upon the injection of Au-PEG-COOH NPs onto DOPC SLVs, a clear and rapid upshift occurs in the frequency signal: from an average (overtones $n = 3$–9) plateau value of −200 ± 20 Hz, it increases to −27.8 ± 3.8 Hz. This is accompanied by a substantial decrease in dissipation: from an average of $(31.8 \pm 1.9) \times 10^{-6}$ to $(5.8 \pm 0.6) \times 10^{-6}$. These (final) plateau values correspond to SLBs containing defects, suggesting that the Au-PEG-COOH NPs can rupture the membrane of zwitterionic vesicles and ultimately form an almost continuous bilayer. After vesicle rupture, the nanoparticles are no longer retained on the surface, as also recently observed in the case of negatively charged CdTe QDs interacting with DOPC SLVs on Au substrates [43].

The injection of Au-PEG-COOH NPs onto partially positively charged DOPC:DOTAP 80:20 SLVs ($\zeta = 14.5 \pm 0.4$ mV) initially causes a frequency decrease, indicating additional NPs' mass gain due to electrostatic attraction (Fig. 6, middle column). Interestingly, between 140 and 150 min along the time axis, a shoulder appears on the declining frequency curve, reflecting a transient mass loss followed by further adsorption. Similar to the pure DOPC system, vesicle membrane rupture occurs also here, however, in a different way. More specifically, the mass loss – attributed to water release due to vesicles rupture – is masked by the continued adsorption of Au-PEG-COOH NPs, driven by electrostatic attraction between them and the remaining positively charged DOPC:DOTAP SLVs. Ultimately, the system evolves into a highly-inhomogeneous and complex structure, composed of bilayer patches, NPs, and intact adsorbed vesicles. This final configuration is characterized by the observed elevated dissipation and overtone spreading (Fig. 6, bottom part of the middle column).

The injection of Au-PEG-COOH NPs onto DOTAP heterogeneous SLBs containing non-ruptured vesicles and bilayer patches with exposed edges (as discussed earlier), produces less pronounced shoulders along the frequency decline (Fig. 6, right column). These small shoulders apparently correspond to the delayed rupture of some – initially intact – adsorbed vesicles. Due to the high positive charge density in DOTAP heterogeneous SLBs, a substantial adsorption of negatively charged Au-PEG-COOH NPs is evidenced by the QCM-D signal. Moreover, the presence of a few remaining intact vesicles, after NPs' injection was completed, effectively increased the available lipid surface for adhesion of NPs. This enhanced interaction resulted to a greater overall NP adsorption, marked by a large final frequency shift of –392 ± 28 Hz. It is worth noting that smaller frequency shifts, of –253 ± 5 Hz, were observed for Au-PEG-COOH NPs interacting with a planar homogeneous DOTAP SLB on SiO_2 substrate (shown in Fig. 1**B**).

Overall, the results show that when SLVs possess high fluidity (i.e. at temperatures well above the main lipid melting transition), negatively charged Au-PEG-COOH NPs effectively target and interact with them often resulting in vesicle rupture. Not only for positively charged (e.g., DOPC:DOTAP) vesicles undergo rupture, but zwitterionic ones do as well. A plausible explanation is the positive charge of the ammonium group at the upper part of phospholipid head, which enables stronger interactions with the negatively-charged Au-PEG-COOH NPs compared to the neutral Au-PEG-OMe ones. It is worth noting that the ripple and gel phases of DOPC, DOPC:DOTAP and DOTAP fall out of the QCM-D temperature range. Thus, in order to further explore the role of lipid phase in the interactions of charged vesicles and NPs, we have employed

DMPC, DPPC and DSPC lipids. Each one of these three zwitterionic lipids was mixed with DOTAP in the following ratios: DMPC:DOTAP 80:20, DPPC:DOTAP 80:20 and DSPC:DOTAP 80:20 respectively. The particular molar ratio in the mixtures was chosen based on two criteria: (a) to induce a positive surface charge density and enable electrostatic attraction with the negatively charged Au-PEG-COOH NPs, and (b) to have a moderate concentration of DOTAP, ensuring that the three lipid vesicle mixtures correspond to the liquid-disordered, the (upper boundary of the) ripple and the gel-ordered phases respectively at 37 °C. Indeed, the main peaks occur around: 18.7 ± 0.5 °C (DMPC:DOTAP 80:20), 37.2 ± 0.5 °C (DPPC:DOTAP 80:20) and 50.3 ± 1.0 °C (DSPC:DOTAP 80:20), as shown in Figure S10 of the Supplementary Material.

Fig. 7 depicts the frequency and dissipation shifts (overtones $n = 3$–9) that occur during the injection of Au-PEG-COOH NPs on SLVs of the three types of mixtures at 37 °C. In all panels of this figure, the initial frequency and dissipation values correspond to the plateau values obtained after the SLV formation. The frequency shifts exhibit larger negative shifts, from DMPC to DPPC to DSPC, in accordance with the vesicles' increased stiffness. Regarding dissipation, DSPC:DOTAP SLVs – in the gel phase – exhibits the highest ΔD_n. The lowest dissipation occurs for DPPC:DOTAP 80:20 SLVs at the upper boundary of the ripple phase, rather than for DMPC:DOTAP in the liquid phase. Notably, a chain length disparity – of two carbon atoms – exists between DPPC and DOTAP, compared to four carbon atoms between DMPC and DOTAP. Larger differences in the chain length can lead to a hydrophobic mismatch within the bilayer, introducing local thickness fluctuations and lateral heterogeneity. As a result, DMPC:DOTAP SLVs – despite their more fluid character – display larger dissipation shifts than DPPC:DOTAP SLVs.

As shown earlier in Fig. 2, in the absence of net electric charge, pure zwitterionic DMPC SLVs remained essentially intact upon the injection of Au-PEG-OMe NPs, while the membrane of DPPC and DSPC vesicles ruptured. With the introduction of electric charge in both SLVs and NPs (by mixing positively charged DOTAP with DMPC, DPPC and DSPC, as well as using negatively charged Au-PEG-COOH NPs), the frequency and dissipation responses changed markedly as shown in Fig. 7. For all partially charged SLVs, an initial decrease in the frequency and increase in the dissipation signals are observed right after injection. DMPC:DOTAP 80:20 and DPPC:DOTAP 80:20 exhibited large frequency downshifts, with a tiny – yet detectable – discontinuity at the early stage of the NPs injection for DMPC:DOTAP, and a more visible change of slope for DPPC:DOTAP. This likely indicates a minor localized vesicle rupture in both cases, with the rupture being slightly larger in the DPPC:DOTAP layer, as evidenced by a clear change in the $\Delta f_n/n$ slope, and a spreading of the ΔD_n curves. For DSPC:DOTAP 80:20, a smaller frequency shift, accompanied by a pronounced superimposed shoulder, appeared – suggesting substantial vesicle rupture concurrent with the NPs' mass gain. The overall shift reflected the balance between mass loss (lipids and buffer) and mass gain (NPs). After the final plateaus were reached, the average frequency shifts (of overtones $n = 3$–9) were –356 ± 44 Hz (DMPC:DOTAP), –390 ± 19 Hz (DPPC:DOTAP), and –83 ± 23 Hz (DSPC:DOTAP). The similar responses of DMPC:DOTAP (in the liquid phase) and DPPC:DOTAP (at the upper boundary of the ripple phase) reflected this phase behavior. As previously observed in the case of SLVs and NPs without electric charge, a greater vesicle membrane bending rigidity correlates with a higher rupture tendency.

To investigate the influence of the lipid phase on the observed behavior, the interactions of DPPC:DOTAP (80:20) SLVs with Au-PEG-COOH NPs were tested at three temperatures, 20 °C, 37 °C, and 50 °C, corresponding to the gel-ordered, the upper boundary of the ripple, and

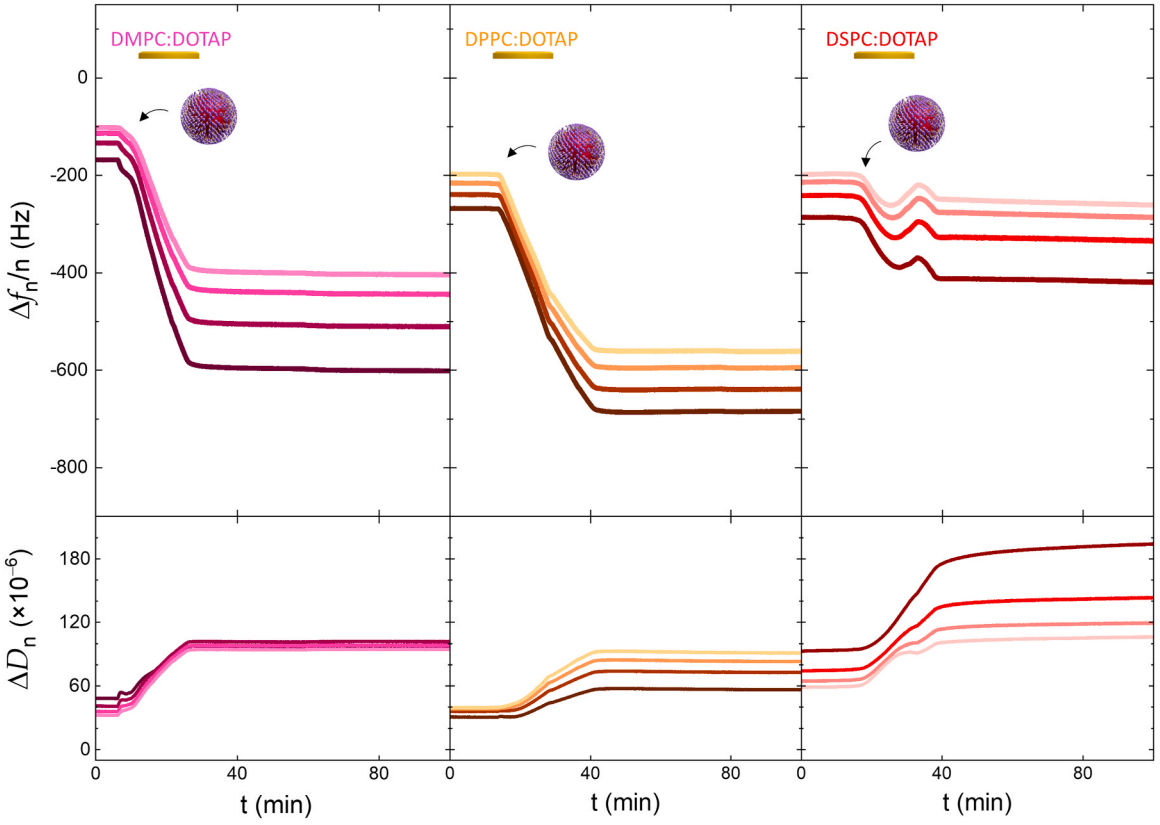

Fig. 7. The interactions of negatively-charged Au-PEG-COOH NPs with DMPC:DOTAP 80:20 (pink color, left column), DPPC:DOTAP 80:20 (orange color, central column), and DSPC:DOTAP 80:20 (red color, right column) SLVs on Au substrates are depicted. The changes in $\Delta f_n/n$ (upper part) and ΔD_n (lower part) were recorded for overtones 3–9, with the color gradients of the curves corresponding to these overtones; darkest (lightest) color corresponds with $n = 3$ ($n = 9$) overtone. For SLVs, 100 nm vesicles were injected at 0.5 mg/mL, whereas the NPs were injected at 0.2 mg/mL; both steps were performed at 37 °C, using a flow rate of 50 μL/min.

the liquid-disordered phases respectively. Fig. 8 displays the resulting frequency and dissipation shifts following the injection of Au-PEG-COOH NPs. A striking contrast exists between the data collected in the gel phase and those in the more fluid phases. At 37 °C and 50 °C, the frequency curves exhibit profiles characteristic of additional mass adsorption. In contrast, at 20 °C, the curve displays a distinct V-shaped dip, reflecting two competing effects: buffer release and lipid loss on one hand and nanoparticle mass gain on the other. These findings further support our conjecture, from the non-charged systems, that the membrane rigidity significantly influences vesicle rupture. Nonetheless, minor slope irregularities at 37 °C and 50 °C indicate that subtle membrane disruptions can still occur in the liquid phase, however, to a much lesser extent compared to the gel phase.

4. Discussion

It is shown in this work that the electrostatic forces played – as expected – a major role in the interactions between different types of supported model membranes (planar and vesicular) and Au NPs. Their long-range nature not only precedes but often facilitates the localized short-range interactions. Starting from SLBs, shown in Fig. 1, strong interactions were observed for charged systems (SLBs and NPs), contrary to neutral systems, where only mild non-specific interactions occurred. This is in agreement with other studies, underlining the role of charge in the rupture of positively charged GUVs by negatively-charged NPs, as well as in the adsorption of negatively charged NPs on (positive) DOTAP but not on (negative) DOPG vesicles [13,46,47].

Upon adsorption of Au-PEG-COOH NPs, the frequency shifts in Fig. 1 do not follow a linear dependence on the amount of charge, as seen by comparison of the plateau values for DOPC, DOPC:DOTAP 50:50, and DOTAP SLBs. In particular, DOPC:DOTAP plateau is closer to the one of DOTAP. A similar observation has been reported by Zhang et al. [25], and it was attributed to the electrostatic repulsion between the cationic TAP groups of DOTAP and positively charged choline of DOPC. More specifically, this repulsion between the two cationic groups induces a reorientation of the DOPC headgroup, which in turn exposes more its choline moiety to the aqueous phase. This conformational change renders the bilayer more positively charged than expected at a given composition [11,12]. Our ζ potential measurements for vesicles (Table S2 in the Supplementary Material) are in line with such a scenario.

An interesting observation in the present work is that the negatively-charged Au-PEG-COOH NPs do also interact with zwitterionic SLVs, despite the overall neutral charge of the latter in our experimental conditions. As shown in Fig. 6, the Au-PEG-COOH NPs cause vesicle rupture in the case of zwitterionic DOPC SLVs. A plausible explanation originates from the dipolar nature of the PC head group, which contains a negatively-charged phosphate and a positively-charged choline moiety. When a negatively charged NP approaches the zwitterionic bilayer, the head group may reorient and elongate perpendicular to the bilayer surface, with the positive choline part extending towards the NP, as calculated by Velikonja et al. [12]. Moreover, small breakthrough forces of 2.7 ± 0.3 nN have been recently reported for DOPC bilayers by atomic force microscopy [48]. Such weak forces, combined with the change in the tilt of the head groups upon NPs' approach, could destabilize the bilayers and make them prone to rupture. This is of particular interest, given that PC lipids are major constituent units of the outer leaflet of mammalian cell membranes. Apart from membrane rupture observed in our case, other effects have also been observed depending on the size and surface chemistry of employed NPs. For instance, Canepa et al. [14] observed a passive permeation of < 6 nm Au NPs (i.e. of smaller core than the ones used in the present work) in POPC vesicles in the liquid-disordered phase. Wang et al. [49] used 20 nm latex NPs and observed a local phase state switch of the bilayers being in close contact with NPs; anionic NPs induced local gelation to the liquid phase of DLPC, whereas cationic ones induced fluidization to the gel phase of DPPC. The gelation effect was always attributed to the reorientation of the lipid head groups [13,50,51].

The present work shows that negatively charged Au-PEG-COOH NPs have strong effects on all three phases (liquid, ripple, and gel) in the case of positively charged SLVs. As it is demonstrated in Fig. 7, although it occurs for all partially charged vesicles, the rupture is largely pronounced in the case of stiffer SLVs. Somewhat opposite trends were revealed in some earlier studies using Au NPs, albeit with different surface chemistry. For example, Sheridan et al. [52] reported a stronger adsorption of citrate-capped Au NPs in the liquid phase of DPPC compared to the gel phase. The effect was attributed to the higher molecular mobility of lipids in the liquid phase, lowering the energetic barriers for NP adsorption and engulfment. A similar explanation was adopted by Cardellini et al. [53] to explain the dependence of citrate-capped Au NPs' adhesion on the lipid stiffness. However, the citrate is not firmly adhered on the NPs' surface and can be easily displaced upon close contact with the bilayer, rendering the NPs 'bare' regarding strong short-range interactions [46]. This leads to a greater tendency for aggregation following the membrane binding. Notably, Cardellini et al. [53] and Sugikawa et al. [51] confirmed that this phenomenon occurs specifically when the lipids are in the liquid phase, but not in the gel phase. Apparently, the different chosen surface chemistry in these studies is the reason behind the opposite trends.

In the case of negatively charged Au-PEG-COOH NPs, vesicle rupture

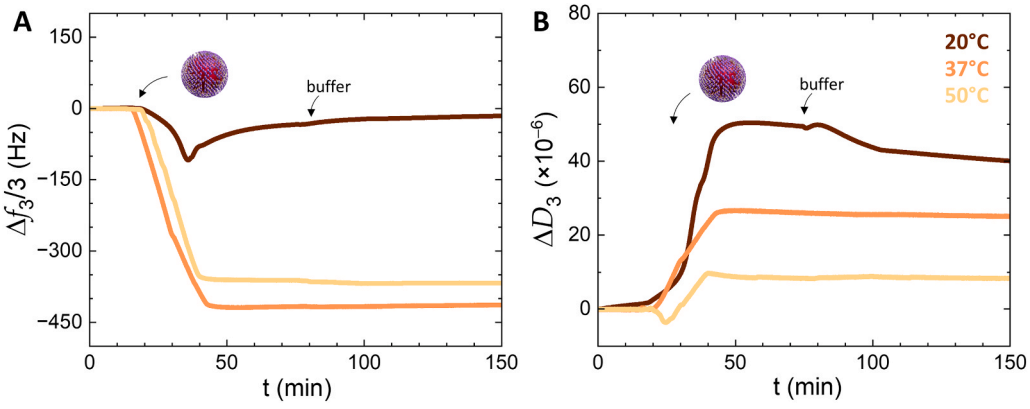

Fig. 8. The temperature influence on the charged SLVs and NPs interactions is depicted. $\Delta f_3/3$ (panel A) and ΔD_3 (panel B) curves are obtained by injecting Au-PEG-COOH NPs on DPPC:DOTAP 80:20 SLVs, adsorbed on Au quartz sensors at 20 °C (brown curves, SLVs in gel-ordered phase), 37 °C (orange curves, SLVs at the boundary of the ripple phase), and 50 °C (yellow curves, SLVs in liquid-disordered phase). The NPs were injected at a concentration of 0.2 mg/mL in Tris buffer, using a flow rate of 50 μL/min.

occurred even for small amounts of charged membrane components (**20%** DOTAP). Our findings are in agreement with other studies, such as of Cao et al. [54], who explored the interactions of anionic DOPC:DOPG GUVs with positively-charged NPs, varying the amount of charge of both system components. Their phase diagram demonstrated that sufficient charge present on at least one of the components was necessary for strong electrostatic attractions to induce vesicle membrane rupture. For fully charged NPs and DOPC:DOPG 80:20, vesicle rupture was observed similar to our case for DSPC:DOTAP 80:20, and to a lesser extent for DPPC:DOTAP 80:20 and DMPC:DOTAP 80:20, as shown in Fig. 7. It is worth noting that, in DPPC:DOTAP and DSPC:DOTAP mixtures, the two lipids are in different phases: DOTAP in liquid, whereas DPPC and DSPC on ripple and gel phases respectively. Therefore, some local phase separation could occur between more-fluid-like and more-gel-like regions of the bilayer, as reported for DSPC and DPPC mixed with DOTAP [55]. The effective acyl-chain length differs between the gel and liquid phases. In the gel phase, acyl chains are ordered and extended, producing a thicker bilayer, whereas in the liquid phase, they are disordered and mobile, yielding a thinner bilayer. Boundaries between regions of differing composition – thus also packing and bilayer thickness – exhibit defects such as exposed hydrophobic parts. Thickness mismatch can occur even when lipids share the same chemical chain length but are in different phases. NPs, in turn, primarily target defects for energetic reasons; this targeting behavior has been predicted by numerical simulations [56] and confirmed experimentally [26,43]. Moreover, the aforementioned regions (TAP-rich and PC-rich) bear a different amount of charge, which could explain the differences in frequency signal profiles observed at the early stage of NPs' injection between Fig. 5 and Fig. 8. At 20 °C in particular, in the case of zwitterionic DPPC vesicles (gel phase) one notices a simple yet direct vesicle membrane rupture. In contrast, in the case of DPPC:DOTAP vesicles, one notices an initial mass gain step, attributed to a preferential, charge-driven targeting of TAP-rich regions by Au-PEG-COOH NPs, followed by the subsequent vesicle rupture driven by the stiff, PC-rich regions.

A very intriguing finding of the present study is that vesicle's membrane rupture occurred in the case of non-charged Au-PEG-OMe NPs and zwitterionic SLVs, which – for example – was not observed in the phase diagram of Cao et al. [54], but can be theoretically explained by the results presented in [11,12]. Moreover, rupture occurs in stiff SLVs, as shown in Fig. 2, for DSPC in the gel phase and for DPPC in the ripple phase. A theoretical explanation of this unforeseen outcome originates from the work of Van der Pol et al. [57], who analyzed the role of lipid phase on the amount of membrane defects *via* coarse-grained simulations. Membrane defects, also referred to as exposed hydrophobic areas, are biologically relevant because they reduce the energetic barrier for membrane protein insertion; proteins preferentially target curved membrane areas where more defects are present. Van der Pol et al. [57] calculated the defect constant π, i.e. the average size of lipid-packing defects along the membrane surface. In flat membranes, π is greater in the liquid phase, due to the decreased tail order; by contrast, in positively curved membranes, π is higher in the gel phase. For DPPC, in particular, π was calculated to be **30%** larger in the gel phase than in the liquid phase. Coarse-grained simulations showed that stiff membranes minimize energy by forming large planar facets with few curved edges instead of distributing curvature uniformly. The faceted morphology of vesicles induces domains of high local curvature along the edges, which considerably increase both the number and size of membrane defects. This explains the higher π values calculated in the gel phase [57]. In this context, the size of exposed hydrophobic areas becomes even greater than the size of defects found in fluid membranes.

In general, macromolecules such as proteins and peptides target lipid rafts, of higher stiffness, in biological membranes [58,59]. It was also shown that amyloid-β (Aβ) proteins – involved in Alzheimer disease – were selectively targeting the highly-curved edge domains of zwitterionic vesicles in the gel phase [60]. In a similar manner, NPs apparently target these regions of defects along the 100 nm DSPC and DPPC SLVs.

An additional factor associated to the occurrence of vesicle rupture only in the ripple and gel phases is the reduced membrane elasticity. When the membrane is treated as a continuum elastic body, its deformation results from an interplay between the free energy gained through binding and the free energy cost associated with bending or stretching the membrane. In our case, softer DMCP SLVs can more easily deform and adapt their shape to the adhered Au-PEG-OMe NPs with large 10 kDa-PEG chain spacers, compared to the stiffer DPPC and DSPC counterparts. The latter are apparently too rigid to absorb the impact of repeated stochastic encounters with NPs. Within the Helfrich framework, this behavior can be rationalized by the higher bending modulus of gel-phase bilayers: curvature deformations and wrapping around nanoparticles are energetically very costly in this phase [7,10]. As a result, rather than accommodating stress through elastic bending, gel-phase membranes behave as mechanically rigid, exhibiting a brittle-like response under nanoparticle-induced stress. By contrast, liquid-disordered membranes, with a substantially lower bending modulus κ, can dissipate the imposed stress more efficiently by bending and partially wrapping around the nanoparticles, thus remaining intact.

5. Conclusions

We have presented a systematic investigation of the impact of various lipid phases – liquid-disordered, ripple, and gel-ordered – on the interactions between model membranes (SLBs, SLVs) and Au nanoparticles. Different NP coatings and membrane compositions were chosen: electrically neutral and negatively-charged Au NPs, as well as SLBs and SLVs that were either neutral (i.e. zwitterionic with net zero charge) or bearing a variable positive charge density. Composition and electric charge were both modified in a stepwise approach, and the interactions between Au NPs and SLBs, as well as SLVs, were probed in real-time by QCM-D. Under the chosen experimental conditions, this work highlights the major influence of the lipid phase, as also suggested by few previous studies [53,61], on the interactions' path. More specifically, in the case of SLVs, stronger interactions and vesicle's membrane rupture were observed in the case of stiffer membranes (in the ripple and – even more – in the gel phases). Strikingly, rupture of stiffer vesicles occurred even without net charge at either component, i.e. zwitterionic SLVs and neutral Au-PEG-OMe NPs, as revealed by QCM-D and additionally supported by AFM. Our findings demonstrate that vesicle membrane rupture is governed by the membrane phase state rather than the acyl chain length, as confirmed by reproducible results across the liquid, ripple and gel phases (Fig. 2 and Fig. 5). A plausible explanation relates to the higher defect density in the stiffer 100 nm vesicles, which – as recently proposed – could adopt a faceted shape [54], presenting highly-curved edge domains as target sites for the NPs. The results obtained for components bearing opposite charge also reveal an increased membrane rupture tendency in stiffer vesicles, yet with a more complex pattern due to the NP adsorption that precedes and accompanies the rupture process. Overall, the present findings highlight lipid packing as a key determinant in nanoparticle-membrane interactions, thereby advancing fundamental understanding.

We anticipate this work to trigger further investigations, addressing the effect of the membrane curvature (e.g. by employing SLVs of variable sizes), the size ratio of NPs to SLVs, the NPs' surface chemistry, as well as the SLVs complexity (for example, including cholesterol). This would provide further insights into the NP-membrane interactions, distinguish the importance of the membranes' thermodynamic and electrostatic state, and support the development of theoretical models.

CRediT authorship contribution statement

George Cordoyiannis: Writing – review & editing, Writing – original draft, Supervision, Methodology, Investigation, Formal analysis, Conceptualization. **Aleš Iglič:** Writing – review & editing, Validation, Project administration, Funding acquisition. **Patricia Losada-Pérez:**

Writing – review & editing, Validation, Methodology, Conceptualization. **Miha Škarabot:** Writing – review & editing, Investigation, Data curation. **Raj Kumar Sadhu:** Writing – review & editing, Investigation, Data curation. **Slavko Kralj:** Writing – review & editing, Validation, Methodology, Data curation. **Maja Caf:** Writing – review & editing, Investigation, Data curation. **Marta Lavrič:** Writing – review & editing, Validation, Investigation, Formal analysis, Data curation. **Laure Bar:** Writing – review & editing, Writing – original draft, Validation, Methodology, Formal analysis, Data curation, Conceptualization.

Declaration of Competing Interest

The authors declare that they have no known competing financial interests or personal relationships that could have appeared to influence the work reported in this paper.

Acknowledgements

Authors acknowledge financial support from the Slovenian Research and Innovation Agency (ARIS) projects J2–4447, J3–4502, J2–60047, J2–3043, as well as ARIS programs P1–0125, P2–0089, and P2–0232.

Appendix A. Supporting information

Supplementary data associated with this article can be found in the online version at doi:10.1016/j.colsurfb.2026.115665.

Data availability

Data will be made available on request.

References

[1] L. Yildirimer, N.T.K. Thanh, M. Loizidou, A.M. Seifalian, Toxicology and clinical potential of nanoparticles, Nano Today 6 (2011) 585–607, https://doi.org/10.1016/j.nantod.2011.10.001.
[2] K. Tahara, S. Fujimoto, F. Fujii, Y. Tozuka, T. Jin, H. Takeuchi, Quantum dot-loaded liposomes to evaluate the behavior of drug carriers after oral administration, J. Pharm. 2013 (2013) 1–6, https://doi.org/10.1155/2013/848275.
[3] L. Caselli, L. Paolini, W.-K. Fong, C. Montis, A. Zendrini, J. Cardellini, P. Bergese, D. Berti, The gold nanoparticle–lipid membrane synergy for nanomedical applications, Nanoscale Horiz. 10 (2025) 1863–1881, https://doi.org/10.1039/d5nh00292c.
[4] X. Zhang, G. Ma, W. Wei, Simulation of nanoparticles interacting with a cell membrane: probing the structural basis and potential biomedical application, NPG Asia Mater. 13 (2021) 52, https://doi.org/10.1038/s41427-021-00320-0.
[5] A.M. Farnoud, S. Nazemidashtarjandi, Emerging investigator series: interactions of engineered nanomaterials with the cell plasma membrane; what have we learned from membrane models? Environ. Sci. Nano 6 (2019) 13–40, https://doi.org/10.1039/C8EN00514A.
[6] R. Kariuki, K.A. Mirihana, R. Penman, A. Hung, N. Meftahi, G. Bryant, P. A. Ramsland, K. Voïtchovsky, C.E. Conn, C. Contini, S.J. Bryant, A. J. Christofferson, A. Elbourne, Interactions of nanoparticles with living and synthetic bio-membranes, Chem. Soc. Rev. (2025), https://doi.org/10.1039/D5CS00841G.
[7] R.K. Sadhu, S.R. Barger, S. Penič, A. Iglič, M. Krendel, N.C. Gauthier, N.S. Gov, A theoretical model of efficient phagocytosis driven by curved membrane proteins and active cytoskeleton forces, Soft Matter 19 (2022) 31–43, https://doi.org/10.1039/D2SM01152B.
[8] J. Lin, H. Zhang, Z. Chen, Y. Zheng, Penetration of lipid membranes by gold nanoparticles: insights into cellular uptake, cytotoxicity, and their relationship, ACS Nano 4 (2010) 5421–5429, https://doi.org/10.1021/nn1010792.
[9] B. Lu, T. Smith, J.J. Schmidt, Nanoparticle–lipid bilayer interactions studied with lipid bilayer arrays, Nanoscale 7 (2015) 7858–7866, https://doi.org/10.1039/C4NR06892K.
[10] M. Fošnarič, A. Iglič, D.M. Kroll, S. May, Monte Carlo simulations of complex formation between a mixed fluid vesicle and a charged colloid, J. Chem. Phys. 131 (2009) 105103, https://doi.org/10.1063/1.3191782.
[11] E. Gongadze, A. Velikonja, Š. Perutkova, P. Kramar, A. Maček-Lebar, V. Kralj-Iglič, A. Iglič, Ions and water molecules in an electrolyte solution in contact with charged and dipolar surfaces, Electrochim. Acta 126 (2014) 42–60, https://doi.org/10.1016/j.electacta.2013.07.147.
[12] A. Velikonja, P.B. Santhosh, E. Gongadze, M. Kulkarni, K. Eleršič, Š. Perutkova, V. Kralj-Iglič, N.P. Ulrih, A. Iglič, Interaction between Dipolar lipid headgroups and charged nanoparticles mediated by water dipoles and ions, Int. J. Mol. Sci. 14 (2013) 15312–15329, https://doi.org/10.3390/ijms140815312.
[13] X. Wei, J. Yu, L. Ding, J. Hu, W. Jiang, Effect of oxide nanoparticles on the morphology and fluidity of phospholipid membranes and the role of hydrogen bonds, J. Environ. Sci. 57 (2017) 221–230, https://doi.org/10.1016/j.jes.2017.02.011.
[14] E. Canepa, S. Salassi, F. Simonelli, R. Ferrando, R. Rolandi, C. Lambruschini, F. Canepa, S. Dante, A. Relini, G. Rossi, Non-disruptive uptake of anionic and cationic gold nanoparticles in neutral zwitterionic membranes, Sci. Rep. 11 (2021) 1256, https://doi.org/10.1038/s41598-020-80953-3.
[15] G.M. Cooper, Structure of the Plasma Membrane. The Cell: A Molecular Approach, 2nd Edition, Sinauer Associates, 2000 https://www.ncbi.nlm.nih.gov/books/NBK9898/.
[16] H.I. Ingólfsson, M.N. Melo, F.J. van Eerden, C. Arnarez, C.A. Lopez, T. A. Wassenaar, X. Periole, A.H. de Vries, D.P. Tieleman, S.J. Marrink, Lipid organization of the plasma membrane, J. Am. Chem. Soc. 136 (2014) 14554–14559, https://doi.org/10.1021/ja507832e.
[17] R. Gupta, B. Rai, Effect of size and surface charge of gold nanoparticles on their skin permeability: a molecular dynamics study, Sci. Rep. 7 (2017) 45292, https://doi.org/10.1038/srep45292.
[18] T. Lunnoo, J. Assawakhajornsak, T. Puangmali, *In Silico* study of gold nanoparticle uptake into a mammalian cell: interplay of size, shape, surface charge, and aggregation, J. Phys. Chem. C. 123 (2019) 3801–3810, https://doi.org/10.1021/acs.jpcc.8b07616.
[19] C. Contini, J.W. Hindley, T.J. Macdonald, J.D. Barritt, O. Ces, N. Quirke, Size dependency of gold nanoparticles interacting with model membranes, Commun. Chem. 3 (2020) 130, https://doi.org/10.1038/s42004-020-00377-y.
[20] J. Agudo-Canalejo, R. Lipowsky, Critical particle sizes for the engulfment of nanoparticles by membranes and vesicles with Bilayer asymmetry, ACS Nano 9 (2015) 3704–3720, https://doi.org/10.1021/acsnano.5b01285.
[21] S. Zuraw-Weston, D.A. Wood, I.K. Torres, Y. Lee, L.-S. Wang, Z. Jiang, G.R. Lázaro, S. Wang, A.A. Rodal, M.F. Hagan, V.M. Rotello, A.D. Dinsmore, Nanoparticles binding to lipid membranes: from vesicle-based gels to vesicle tubulation and destruction, Nanoscale 11 (2019) 18464–18474, https://doi.org/10.1039/C9NR06570A.
[22] C. Montis, L. Caselli, F. Valle, A. Zendrini, F. Carlà, R. Schweins, M. Maccarini, P. Bergese, D. Berti, Shedding light on membrane-templated clustering of gold nanoparticles, J. Colloid Interface Sci. 573 (2020) 204–214, https://doi.org/10.1016/j.jcis.2020.03.123.
[23] W. Helfrich, Elastic properties of lipid bilayers: theory and possible experiments, Z. Naturforsch. C. 28 (1973) 693–703, https://doi.org/10.1515/znc-1973-11-1209.
[24] M. Deserno, T. Bickel, Wrapping of a spherical colloid by a fluid membrane, EPL 62 (2003) 767, https://doi.org/10.1209/epl/i2003-00438-4.
[25] X. Zhang, S. Yang, Nonspecific adsorption of charged quantum dots on supported zwitterionic lipid bilayers: real-time monitoring by quartz crystal microbalance with dissipation, Langmuir 27 (2011) 2528–2535, https://doi.org/10.1021/la104449y.
[26] E.S. Melby, A.C. Mensch, S.E. Lohse, D. Hu, G. Orr, C.J. Murphy, R.J. Hamers, J. A. Pedersen, Formation of supported lipid bilayers containing phase-segregated domains and their interaction with gold nanoparticles, Environ. Sci. Nano 3 (2016) 45–55, https://doi.org/10.1039/C5EN00098J.
[27] H. Guo, Q. Xing, R. Huang, D.W. Lee, R. Su, W. Qi, Z. He, Real-time QCM-D monitoring of deposition of gold nanorods on a supported lipid bilayer as a model cell membrane, ACS Omega 4 (2019) 6059–6067, https://doi.org/10.1021/acsomega.9b00287.
[28] Q. Chen, S. Xu, Q. Liu, J. Masliyah, Z. Xu, QCM-D study of nanoparticle interactions, Adv. Colloid Interface Sci. 233 (2016) 94–114, https://doi.org/10.1016/j.cis.2015.10.004.
[29] N. Yousefi, N. Tufenkji, Probing the interaction between nanoparticles and lipid membranes by quartz crystal microbalance with dissipation monitoring, Front. Chem. 4 (2016), https://doi.org/10.3389/fchem.2016.00046.
[30] Q. Wang, Y. Chao, Multifunctional quantum dots and liposome complexes in drug delivery, J. Biomed. Res. 32 (2018) 91–106, https://doi.org/10.7555/JBR.31.20160146.
[31] M.M. Sirch, A. Kamenac, S.V. Neidinger, A. Wixforth, C. Westerhausen, Phase-state-dependent silica nanoparticle uptake of giant unilamellar vesicles, J. Phys. Chem. B 128 (2024) 7172–7179, https://doi.org/10.1021/acs.jpcb.4c02383.
[32] W.-C. Hou, B.Y. Moghadam, C. Corredor, P. Westerhoff, J.D. Posner, Distribution of functionalized gold nanoparticles between water and lipid bilayers as model cell membranes, Environ. Sci. Technol. 46 (2012) 1869–1876, https://doi.org/10.1021/es203661k.
[33] C. Casals, O. Cañadas, Role of lipid ordered/disordered phase coexistence in pulmonary surfactant function, Biochim. Biophys. Acta (BBA) - Biomembr. 1818 (2012) 2550–2562, https://doi.org/10.1016/j.bbamem.2012.05.024.
[34] P. Kesharwani, R. Ma, L. Sang, M. Fatima, A. Sheikh, M.A.S. Abourehab, N. Gupta, Z.-S. Chen, Y. Zhou, Gold nanoparticles and gold nanorods in the landscape of cancer therapy, Mol. Cancer 22 (2023) 98, https://doi.org/10.1186/s12943-023-01798-8.
[35] L. Shi, J. Zhang, M. Zhao, S. Tang, X. Cheng, W. Zhang, W. Li, X. Liu, H. Peng, Q. Wang, Effects of polyethylene glycol on the surface of nanoparticles for targeted drug delivery, Nanoscale 13 (2021) 10748–10764, https://doi.org/10.1039/D1NR02065J.
[36] S.R. Tabaei, J.-H. Choi, G. Haw Zan, V.P. Zhdanov, N.-J. Cho, Solvent-assisted lipid bilayer formation on silicon dioxide and gold, Langmuir 30 (2014) 10363–10373, https://doi.org/10.1021/la501534f.

[37] M. Lavrič, L. Bar, M.E. Villanueva, P. Losada-Pérez, A. Iglič, N. Novak, G. Cordoyiannis, Assessing the quality of solvent-assisted lipid bilayers formed at different phases and aqueous buffer media: a QCM-D study, Sensors 24 (2024) 6093, https://doi.org/10.3390/s24186093.
[38] A.R. Ferhan, B.K. Yoon, S. Park, T.N. Sut, H. Chin, J.H. Park, J.A. Jackman, N.-J. Cho, Solvent-assisted preparation of supported lipid bilayers, Nat. Protoc. 14 (2019) 2091–2118, https://doi.org/10.1038/s41596-019-0174-2.
[39] T. Polajžer, M. Kranjc, S. Kralj, M. Caf, R. Romih, S. Hudoklin, F. Rocca, D. Miklavčič, Limited efficacy of nanoparticle-assisted electroporation for membrane permeabilization and gene electrotransfer, Pharmaceutics 17 (2025) 964, https://doi.org/10.3390/pharmaceutics17080964.
[40] R.K. Sadhu, A. Iglič, N.S. Gov, A minimal cell model for lamellipodia-based cellular dynamics and migration, J. Cell. Sci. 136 (2023) jcs260744, https://doi.org/10.1242/jcs.260744.
[41] R.K. Sadhu, S. Penič, A. Iglič, N.S. Gov, Modelling cellular spreading and emergence of motility in the presence of curved membrane proteins and active cytoskeleton forces, Eur. Phys. J. 136 (2021) 495, https://doi.org/10.1140/epjp/s13360-021-01433-9.
[42] I. Reviakine, D. Johannsmann, R.P. Richter, Hearing what you cannot see and visualizing what you hear: interpreting quartz crystal microbalance data from solvated interfaces, Anal. Chem. 83 (2011) 8838–8848, https://doi.org/10.1021/ac201778h.
[43] L. Bar, F. Perissinotto, L. Redondo-Morata, M.I. Giannotti, J. Goole, P. Losada-Pérez, Interactions of hydrophilic quantum dots with defect-free and defect containing supported lipid membranes, Colloids Surf. B Biointerf. 210 (2022) 112239, https://doi.org/10.1016/j.colsurfb.2021.112239.
[44] N. Bibissidis, K. Betlem, G. Cordoyiannis, F.P. Bonhorst, J. Goole, J. Raval, M. Daniel, W. Góźdź, A. Iglič, P. Losada-Pérez, Correlation between adhesion strength and phase behaviour in solid-supported lipid membranes, J. Mol. Liq. 320 (2020) 114492, https://doi.org/10.1016/j.molliq.2020.114492.
[45] S.-E. Choi, K. Greben, R. Wördenweber, A. Offenhäusser, Positively charged supported lipid bilayer formation on gold surfaces for neuronal cell culture, Biointerphases 11 (2016) 021003, https://doi.org/10.1116/1.4945306.
[46] F. Wang, J. Liu, Self-healable and reversible liposome leakage by citrate-capped gold nanoparticles: probing the initial adsorption/desorption induced lipid phase transition, Nanoscale 7 (2015) 15599–15604, https://doi.org/10.1039/C5NR04805B.
[47] N. Yousefi, A. Wargenau, N. Tufenkji, Toward more free-floating model cell membranes: method development and application to their interaction with nanoparticles, ACS Appl. Mater. Interfaces 8 (2016) 14339–14348, https://doi.org/10.1021/acsami.6b00775.
[48] M.E. Villanueva, L. Bar, L. Porcar, Y. Gerelli, P. Losada-Pérez, Resolving the interactions between hydrophilic CdTe quantum dots and positively charged membranes at the nanoscale, J. Colloid Interface Sci. 677 (2025) 620–631, https://doi.org/10.1016/j.jcis.2024.07.220.
[49] B. Wang, L. Zhang, S.C. Bae, S. Granick, Nanoparticle-induced surface reconstruction of phospholipid membranes, Proc. Natl. Acad. Sci. U. S. A. 105 (2008) 18171–18175, https://doi.org/10.1073/pnas.0807296105.
[50] F. Wang, D.E. Curry, J. Liu, Driving adsorbed gold nanoparticle assembly by merging lipid gel/fluid interfaces, Langmuir 31 (2015) 13271–13274, https://doi.org/10.1021/acs.langmuir.5b03606.
[51] K. Sugikawa, T. Kadota, K. Yasuhara, A. Ikeda, Anisotropic self-assembly of citrate-coated gold nanoparticles on fluidic liposomes, Angew. Chem. Int. Ed. 55 (2016) 4059–4063, https://doi.org/10.1002/anie.201511785.
[52] A.J. Sheridan, K.C. Thompson, J.M. Slater, Interaction of negatively and positively capped gold nanoparticle with different lipid model membranes, Biophys. Chem. 290 (2022) 106896, https://doi.org/10.1016/j.bpc.2022.106896.
[53] J. Cardellini, L. Caselli, E. Lavagna, S. Salassi, H. Amenitsch, M. Calamai, C. Montis, G. Rossi, D. Berti, Membrane phase drives the assembly of gold nanoparticles on biomimetic lipid bilayers, J. Phys. Chem. C 126 (2022) 4483–4494, https://doi.org/10.1021/acs.jpcc.1c08914.
[54] R. Cao, J. Gao, S. Thayumanavan, A. Dinsmore, Triggered interactions between nanoparticles and lipid membranes: design principles for gel formation or disruption-and-release, Soft Matter 17 (2021) 7069–7075, https://doi.org/10.1039/D1SM00864A.
[55] L. Almonte, J. Colchero, True non-contact atomic force microscopy imaging of heterogeneous biological samples in liquids: topography and material contrast, Nanoscale 9 (2017) 2903–2915, https://doi.org/10.1039/C6NR07967A.
[56] R.C. Van Lehn, M. Ricci, P.H.J. Silva, P. Andreozzi, J. Reguera, K. Voïtchovsky, F. Stellacci, A. Alexander-Katz, Lipid tail protrusions mediate the insertion of nanoparticles into model cell membranes, Nat. Commun. 5 (2014) 4482, https://doi.org/10.1038/ncomms5482.
[57] R.W.I. Van Der Pol, B.W. Brinkmann, G.J.A. Sevink, Analyzing lipid membrane defects via a coarse-grained to triangulated surface map: the role of lipid order and local curvature in molecular binding, J. Chem. Theory Comput. 20 (2024) 2888–2900, https://doi.org/10.1021/acs.jctc.4c00082.
[58] T. Garofalo, R. Misasi, G. Preta, Editorial: targeting lipid rafts as a strategy against infection and cancer, Front. Cell Dev. Biol. 9 (2021), https://doi.org/10.3389/fcell.2021.748905.
[59] M. Warda, S. Tekin, M. Gamal, N. Khafaga, F. Çelebi, G. Tarantino, Lipid rafts: novel therapeutic targets for metabolic, neurodegenerative, oncological, and cardiovascular diseases, Lipids Health Dis. 24 (2025) 147, https://doi.org/10.1186/s12944-025-02563-0.
[60] Y. Sugiura, K. Ikeda, M. Nakano, High membrane curvature enhances binding, conformational changes, and fibrillation of Amyloid-β on lipid bilayer surfaces, Langmuir 31 (2015) 11549–11557, https://doi.org/10.1021/acs.langmuir.5b03332.
[61] F.G. Strobl, F. Seitz, C. Westerhausen, A. Reller, A.A. Torrano, C. Bräuchle, A. Wixforth, M.F. Schneider, Intake of silica nanoparticles by giant lipid vesicles: influence of particle size and thermodynamic membrane state, Beilstein J. Nanotechnol. 5 (2014) 2468–2478, https://doi.org/10.3762/bjnano.5.256.